

- sapem: Dispersion relations of guided acoustic waves in poroelastic-based multilayer structures

1 Abstract

A method is developed to solve the dispersion of guided waves in multilayer structures with layers of arbitrary nature. The governing equations of each layers are discretized using a spectral collocation method and solved as a generalized eigenvalue problem, which yields a complex wavenumbers, allowing to present dispersion diagrams, as well as eigenvectors, representing all mode shapes from the involved physical fields in each layer. A focus is made on poroelastic layers, which present a lot of dissipations. Usually, root-finding method for dispersion problems are very limited when it comes to wave lossy propagation. The present method overcomes these issues, ensuring also to retrieve all solutions and also allows accounting for outgoing wave radiation. Further analysis on the dispersion properties of an elastic-poroelastic bilayer structure is done and additional tools are developed to calculate the decoupled solid and fluid phases Umov-Poynting vectors in poroelastic layers. The validity of the method is supported by root-finding solutions as well as experimental data from measurements on the bilayer.

2 Introduction

The mechanisms of losses in poroelastic materials provide interesting physical effects, mainly for acoustic absorption. It is of interest to study how these lossy materials affect acoustic and elastic waves propagating therein. However, there are scarce results and investigations on wave dispersion in poroelastic media [1–4]. Therefore, we propose to develop a numerical method to reliably compute dispersion diagrams in such materials, that is to solve complex wavenumbers \tilde{k}_1 for a set of frequencies ω .

Common methods rely on root-finding algorithms to locate analytical complex roots of complex matrix determinants or of characteristic equations. One efficient

way to do so is to use the Müller method [5] which is a secant-based complex root-finding algorithm. For well-conditioned problems, it can be relevant to consider root-finding-based algorithms [6–8]. However, these methods usually require multiple values to initialise the root computation algorithm which is a predicament: depending on those initial values, the local minima in the function, and the numerical conditioning of the matrix, some areas of the wavenumber-frequency space can be difficult to solve.

Spectral methods are a class of numerical methods, which can be used to solve various wave radiation problems [9]. Using such method for the solution of wave dispersion, emerged in the last decades. Different elastic waves propagation configurations are well-studied in the literature. Classical Lamb waves in a free elastic plate were studied in Ref.[10]. In recent years, the spectral collocation method was especially used for different cases including layered annulii [11, 12]. In the case of anisotropic elastic materials, Quintanilla *et al.* provided an implementation of this method to solve multilayer configurations [13]. Also, some configurations with fluid-coupled elastic layers, leading to the emergence of leaky modes, are studied through different ways. The modal analysis of analogous configurations can model the surrounding fluid using perfectly matched layers [14]. It can also be considered as an adjacent domain thus using spectral methods for the discretization of all elements of the geometry [15] into a finite domain. Only a local interaction can be considered, leading to a non-linear eigenvalue problem [16].

Another method, the semi-analytical finite elements method (SAFE) is used for configurations akin to those seen for spectral methods. The procedure used in SAFE methods consists in a finite elements discretization with harmonic functions along the main propagation direction [17, 18]. FEM is also used for the modal analysis of multilayer waveguides [19].

Multilayer configurations have long been investigated [20, 21] and more recently regarding multilayer media with arbitrary layers, using transfer matrices [22] or stiffness matrices [23].

In this work, we propose to investigate a SCM allowing to solve general configuration of multilayer structures composed of fluid, elastic or poroelastic layers, via

discretization of the relevant set of equations. Outgoing wave radiation in an infinite fluid medium is accounted from the method developed by [16].

This paper will be divided in three sections. First, we will develop the method to write the SCM for general multilayer configurations and how each layer is coupled with each other. Then, the example case of a bilayer elastic-poroelastic structure will be studied specifically. We will see its dispersion diagram, with the numerical solution compared to what is obtained with classical methods. Mode shapes are associated to the solved wavenumbers, corresponding to the physical fields involved in the problem. Umov-Poynting will be calculated from the spectral solutions also, providing insight on the repartition of the energy in the poroelastic material. Finally, an experimental confrontation is provided using the same bilayer structure.

3 Description of the method

The problem of interest in this paper is the matter of the dispersion behavior of guided waves propagating along an arbitrary multilayered system. The procedure is derived hereafter and makes use of the so-called spectral collocation method (SCM).

3.1 Guided waves in a multilayer structure

The geometry of the considered structure is described hereunder. Let N stacked layers with domains denoted as Ω_n , with $n = 0 \dots N$, and thicknesses h_n . The total structure thickness is $H = \sum_n h_n$. Each layer is coupled to its neighbors by interface conditions Γ_n located at the top and at the bottom, e.g. the interfaces of Ω_n are Γ_{n-1} and Γ_n and Γ_0 is the interface between Ω_{0-} and Ω_1 . The top and bottom frontiers of the structure are denoted Γ_0 and Γ_N and act as the whole structure interfaces: if one consider a radiating medium, a coupling condition is imposed at $\Omega_{0\pm}$. Otherwise, in the case of free or rigid boundaries, the appropriate conditions are assumed. The description of the geometry is summarized in Fig.(1a). Note that the nature of each layer of material is arbitrary: as a general description, each layer n is described by a set of P_n fields involved in the motion equations governing the propagation of waves in the said layer. In the n -th layer, the set of fields is written

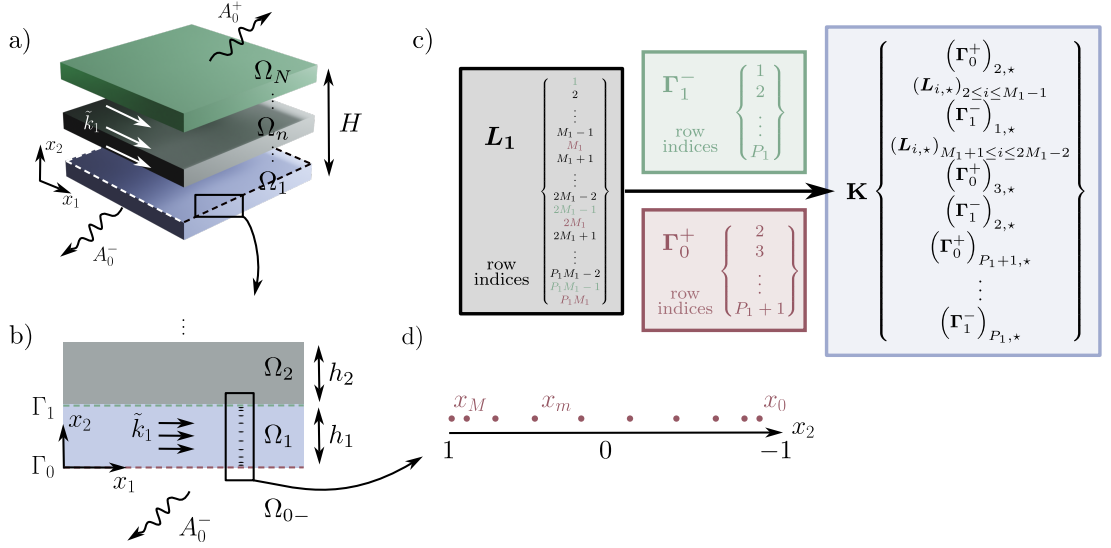


Figure 1: Diagram of the general geometry with a) the stack of arbitrary layers with the amplitudes A_0 of radiated waves from each end of the structure, b) a close-up of the first two layers with their interface Γ_1 and c) the pattern of the discretization nodes along the x_2 axis with an arbitrary value $M = 10$ for representation. d) Diagram representing the procedure for the numerical scheme by combining both the residual matrix and the coupling matrices.

as $\mathbf{s}_n = (\mathbf{s}_{n,0}, \dots, \mathbf{s}_{n,P_n})$.

This work focuses on guided plane waves, propagating in the structure along the positive x_1 direction. Any field in the system is written as the ansatz

$$\mathbf{s}(\mathbf{x}, \omega) = \mathbf{s}(x_2) e^{ik_1 x_1} e^{-i\omega t}. \quad (1)$$

Thus, the propagation of the fields in the problem only depend on the transverse x_2 axis. In order to solve this univariate field, a discretization is applied on the physical axis.

3.2 Spectral collocation method on a single arbitrary layer

The propagation inside one layer Ω_1 is described in this section, restricting our considerations to a domain $x_2 \in [0, h_1]$. The motion equations governing the set of

fields \mathbf{s}_1 are discretized following the procedure detailed hereunder. The index 1 is dropped for clarity? Coupling conditions are applied to the fields \mathbf{s} at the top and at the bottom, denoted respectively Γ_1 and Γ_0 . The geometry is shown in Fig.(1b).

Spectral methods are a powerful tool for spatial discretization [24, 25]. Generally, each field is expanded into a polynomial and truncated at order M . The polynomial basis that is used here and more generally in spectral collocation methods (SCM) are Chebyshev polynomials. The approximated fields are written as

$$\mathbf{s}(x_2) \approx \sum_{i=0}^P \boldsymbol{\alpha}_i(x_j) \psi_i(x_2), \quad (2)$$

with $\boldsymbol{\alpha}(x_j)$ the coefficients of the polynomial expansions. ψ_i are i -th order basis functions, chosen as Chebyshev polynomials. A set of points describes the discretization of the layer, onto which a residue is imposed at each of the nodes. Since this is a collocation method, the residue is set to vanish at each node.

The sets of nodes $\{\underline{x}_j\} = \cos\left(\frac{j\pi}{M}\right), j = 0 \dots M$ to be used are called Chebyshev nodes [25] and represent the roots of the aforementioned polynomials. The collocation points are the locii of the nodes with indices $j = 1 \dots M - 1$, and thus the residue writes as

$$\sum_j \mathcal{L}[T_m](\underline{x}_j) \mathbf{s}^{(n)} = 0, \quad (3)$$

with the linear operator \mathcal{L} the acts on the fields as the governing motion equations. The residue equations can be arranged in matrix form, denoted $\underline{\underline{\alpha}}$. On the remaining nodes, boundary or interfaces conditions are written

The numerical solution of this type of problem usually makes use of differentiation matrices (DMs) [11, 26] denoted as $\underline{\underline{D}}_2$ the first-order DM along x_2 and $\underline{\underline{D}}_{22}$, the second-order DM. This is an efficient numerical implementation [27] of the expression of Chebyshev polynomials expressed at Chebyshev nodes, and thus there are as much nodes as polynomials, M . Hence These matrices are square with size $(M \times M)$ and the number of nodes chosen to discretize is identical to the number of Chebyshev polynomials. The formulation also prevents the occurrence of roundoff errors [28], which especially of importance for spectral methods applied to eigenvalue problems [ref?]. Applying DMs to this system is quite straightforward and leads to

rewriting the derivatives of the field \underline{s} as

$$\begin{aligned}\mathbf{s}(x_j) &\rightarrow \underline{\underline{I}} \underline{s}(x_2); \quad \partial_2 \mathbf{s}(x_j) \rightarrow \left(\frac{2}{h}\right) \underline{\underline{D}_2} \underline{s}(x_2) \\ \partial_{22} \mathbf{s}(x_j) &\rightarrow \left(\frac{2}{h}\right)^2 \underline{\underline{\underline{D}}}_{22} \underline{s}(x_2).\end{aligned}\tag{4}$$

with the underlined variables representing discrete vectors and the double underscore, discrete matrices, instead of the bold typesetting for continuous fields and matrix expressions. The 2 subscript denotes differentiation along x_2 and $\underline{\underline{I}}$ is the identity matrix, used for pointwise multiplication to express the field with the same dimension as the derivatives. The normalization of the DMs is $(2/h)^k$ corresponding to the mapping from physical space $[0, h]$ to the "spectral" domain $[-1, 1]$. The normalization factors are omitted for the sake of simplicity. Note that differentiating along x_1 is straightforward, $(\partial_1)^k \mathbf{s} = (i\tilde{k}_1)^k \mathbf{s}$. Finally, the residue matrix have a size $(P_n M_n + 1, P_n M_n + 1)$.

In order to apply the interface/boundary conditions, the rows of $\boldsymbol{\alpha}_1$ at $M_1, 2M_1, \dots, P_1 M_1$ is removed to put on the rows of the lower interface Γ^- and the rows at $M_1+1, 2M_1+1, \dots, P_1 M_1 + P_2 M_2$ to account for the upper interface Γ^+ . This is because the generation of differentiation matrices span the whole discretized grid but the edge nodes are involved in enforcing coupling with other layers or boundary conditions. The interface matrix $\boldsymbol{\Gamma}$ is split into two part, relating the equation terms for the fields in the upper domain with $\boldsymbol{\Gamma}^-$ and the lower with $\boldsymbol{\Gamma}^+$. These two matrices satisfy generally

$$\boldsymbol{\Gamma}_n^- \mathbf{s}_n + \boldsymbol{\Gamma}_n^+ \mathbf{s}_{n+1} = \mathbf{0}\tag{5}$$

Finally, the system for a single layer writes as

$$\underbrace{\begin{pmatrix} \boldsymbol{\Gamma}_0^- & \boldsymbol{\Gamma}_0^+ & \mathbf{0} \\ \mathbf{0} & \boldsymbol{\alpha}_1 & \mathbf{0} \\ \mathbf{0} & \boldsymbol{\Gamma}_1^- & \boldsymbol{\Gamma}_1^+ \end{pmatrix}}_{\boldsymbol{\kappa}} \underbrace{\begin{pmatrix} A_0^- \\ \mathbf{s}_1 \\ A_0^+ \end{pmatrix}}_{\mathbf{s}} = \mathbf{0}\tag{6}$$

Fluid-coupling with the edges of the structure is accounted at the interfaces Γ_0 and Γ_N , as a local interaction. An additional amplitude term is provided to account for radiation in the infinite medium. The procedure is explained in greater details

in Kiefer *et al.*[16]. Wave propagation is described as a single radiated wave. After a spatial Fourier transform, the pressure fields are written, at the bottom layer In the case of a surrounding medium, the radiated wave is assumed to be harmonic, i.e,

$$p_{0-} = A_{0-} e^{-ik_2^0 x_2} e^{ik_1 x_1}, \quad x_2 \in [0, -\infty], \quad (7)$$

$$p_{0+} = A_{0+} e^{ik_2^0 (x_2 - H)} e^{ik_1 x_1}, \quad x_2 \in [H, +\infty]. \quad (8)$$

3.3 Extension to multilayer

Now we consider the complete multilayer system. The procedure derived in the previous paragraph is extended to all domains and interfaces involved in the structure. The global physical fields vector writes then as $\mathbf{S} = (\mathbf{s}^{(0)} \ \dots \ \mathbf{s}^{(N)})$.

The total size of the problem is $\sum_{n=0}^N M_n P_n + 2$. The total number of interface conditions to write in the system is $\sum_{n=0}^N P_n + 2$.

For each layer, the motion equations are stored in matrices denoted as $\boldsymbol{\alpha}_n$, storing the residual equations. Each of these matrix has a size $P_n(M_n - 2)$ and is filled according to Eq.(3) with interface conditions ordered in the same way as Fig.(1d).

The boundary conditions between two layers n and $n + 1$ are implemented as before, written as $\boldsymbol{\Gamma}_n$. The width of these interface matrices are $P_n + P_n + 1$ and the superscript specifies which physical fields it is applied to. That is, $\boldsymbol{\Gamma}_n^- = \boldsymbol{\Gamma}_n(0 \dots I_n)$ and $\boldsymbol{\Gamma}_n^+ = \boldsymbol{\Gamma}_n(I_n \dots I_n + I_{n+1})$. The system writes as

$$\boldsymbol{\Gamma}_n^- \mathbf{s}_n + \boldsymbol{\Gamma}_n^+ \mathbf{s}_{n+1} = \mathbf{0}. \quad (9)$$

$$\mathbf{S} = (A_{0-} \ \mathbf{s}^{(1)} \ \mathbf{s}^{(2)} \ \dots \ \mathbf{s}^{(N)} \ A_{0+})^T. \quad (10)$$

$$\mathbf{K} \mathbf{S} = \begin{pmatrix} \boldsymbol{\Gamma}_0^- & \boldsymbol{\Gamma}_0^+ & 0 \\ 0 & \boldsymbol{\alpha}_1 & 0 \\ 0 & \boldsymbol{\Gamma}_1^- & \boldsymbol{\Gamma}_1^+ & 0 \\ & 0 & \boldsymbol{\alpha}_2 & 0 \\ & \ddots & \ddots & \ddots \\ & 0 & \boldsymbol{\alpha}_N & 0 \\ 0 & \boldsymbol{\Gamma}_N^- & \boldsymbol{\Gamma}_N^+ \end{pmatrix} \begin{pmatrix} A_{0-} \\ \mathbf{s}^{(1)} \\ \mathbf{s}^{(2)} \\ \vdots \\ \mathbf{s}^{(N)} \\ A_{0+} \end{pmatrix} = \mathbf{0}. \quad (11)$$

This numerical scheme is an arrangement of several blocks of the system written in Eq.(6). For a given layer n described by $\boldsymbol{\alpha}_n$ with size $((M_n - 2)P_n, P_n M_n)$, the upper coupling matrix Γ_n has size $(P_n + P_{n+1}, P_n M_n + P_{n+1} M_{n+1})$ and its component for \mathbf{s}_n is Γ_n^- (size).

The matrix derived in this section is similar to what was done for other multilayer configurations[13] but the chosen approach is more general and does not restrict to a specific class of materials. As an example, one sets layers with $P_n = 2$ for an elastic layer (displacement vector with x_1 and x_2 components), for a fluid, $P_n = 1$ (sole pressure field) and in a poroelastic layer, $P_n = 3$ (both displacement vectors and a pressure field). In the upcoming section, example of structures and, the way to write the matrix $\boldsymbol{\alpha}$ for the afore mentioned material types is derived. Appendices A and B contains the expression of these matrices for poroelastic and elastic layers, respectively.

3.4 Nonlinear eigenvalue problem

At this point, the numerical scheme has been written and can be solved using the procedure described in [16]. The scheme matrix $[\mathbf{K}]$ is decomposed depending on wavenumber orders, thus leading to

$$\left(k_1^2 \mathbf{K}_2 + k_1 \mathbf{K}_1 + \mathbf{K}_0 + ik_2^{(0)} \mathbf{K}'_1 \right) \mathbf{S} = \mathbf{0}, \quad (12)$$

with $k_2^{(0)} = \sqrt{k^{(0)2} - k_1^2}$. The derived eigenvalue problem is nonlinear due to the k_2 term, which resembles the *gun* problem [29]. The linearization is done by a change of variable $k_1 = k^{(0)}(\gamma + \gamma^{-1})/2$ and $k_2 = k^{(0)}(\gamma - \gamma^{-1})/2i$ [30]. The details of further calculations can be found in the work of Kiefer *et al.*[16]. After companion linearization, a generalized eigenvalue problem can be solved using traditional solvers and written as

$$(\mathbf{A}' - \gamma \mathbf{B}') \mathbf{S}' = \mathbf{0}. \quad (13)$$

The Matrices \mathbf{A}' and \mathbf{B}' contain the previously derived numerical scheme, with size $(4 \cdot P_n M_n + 2, 4 \cdot P_n M_n + 2)$ and eigenvectors $\mathbf{S}' = (\gamma^3 \mathbf{S} \quad \gamma^2 \mathbf{S} \quad \gamma \mathbf{S} \quad \mathbf{S})^T$.

4 Bilayer structure

In this section, a composite structure of 2 layers is studied to illustrate the previously derived method, and to gain some insights on its modal behaviour. The studied configuration is an aluminium plated poroelastic layer with a rigid backing. Both simulation and experimental results will be investigated. As a preliminary step, the study of the dispersion of guided waves in a poroelastic plate with both side fluid-coupled is detailed in Appendix A.

4.1 Numerical scheme

The procedure to write the numerical scheme for the SCM is provided in the previous section. Thus, we have in this case $N = 2$. The diagram for the structure is provided in Fig. (2a). Each domain is discretized using collocation points, as before and the layers have a number of physical domains of $I_1 = 3, I_2 = 2$ from bottom to top, as they are respectively poroelastic and elastic, denoted by superscript (p) and (e) . In total, there are 5 physical fields to solve in this structure, which are $u_1^{(e)}, u_2^{(e)}, u_1^{(p)}, u_2^{(p)}$ and $p^{(p)}$. There is an additional amplitude term to account for: an acoustic wave radiates towards infinity at the upper interface.

The motion equations in an elastic medium are derived from the fundamental elasticity equations [31],

$$\rho\omega^2\mathbf{u} + (\lambda + 2\mu)\nabla(\nabla \cdot \mathbf{u}) + \mu\nabla^2\mathbf{u} = 0, \quad (14)$$

and its discretized form is denoted $\boldsymbol{\alpha}^{(e)}$. Its expression is described in Appendix B.

The motion equations for the propagation of a displacement field in an elastic medium originates from the elastodynamic equation written in Eq.(14) and can be discretized into the following matrix

$$\boldsymbol{\alpha}^{(e)}\mathbf{u}^{(e)} = \left[\rho^{(e)}\omega^2\mathbf{T} + \begin{pmatrix} -k_1^2(\lambda + 2\mu)\mathbf{T} + \mu\mathbf{T}_{22} & ik_1(\lambda + \mu)\mathbf{T}_2 \\ ik_1(\lambda + \mu)\mathbf{T}_2 & (\lambda + 2\mu)\mathbf{T}_{22} - k_1^2\mu\mathbf{T} \end{pmatrix} \right] \mathbf{u}^{(e)} = 0. \quad (15)$$

The layer below the elastic plate is a poroelastic material (PEM) whose behaviour is described by the Biot theory [32, 33]. This material is biphasic and is made of

a solid matrix embedding a fluid phase filling its pores. The original formulation accounts for the displacement fields in the skeleton \mathbf{u}^s and the displacement fields inside the fluid \mathbf{u}^f . However, here the physical fields of interest of the PEM are the displacement field of the skeleton $\underline{\mathbf{u}}^s$ and the pressure field in the fluid p . The $(\underline{\mathbf{u}}^s, p)$ formulation was derived by Atalla *et al.*[34] for numerical stability and a use towards FEM.

The motion equation describing the poroelastic material are written as

$$\begin{aligned}\nabla \cdot \hat{\boldsymbol{\sigma}}^s + \tilde{\rho}\omega^2 \mathbf{u}^s + \tilde{\gamma} \nabla p &= 0, \\ \frac{\nabla^2 p}{\tilde{\rho}_{22}\omega^2} - \frac{\tilde{\gamma}}{\phi^2} \nabla \cdot \mathbf{u}^s + \frac{1}{\tilde{R}} p &= 0,\end{aligned}\tag{16}$$

where the solid stress tensor being $\hat{\boldsymbol{\sigma}}^s = \hat{A} \nabla \cdot \mathbf{u}^S \mathbf{I} + 2N_s \boldsymbol{\epsilon}^s$. The coefficients are explicated in Appendix A and depend on the dynamic density $\tilde{\rho}_{eq}(\omega)$ and bulk modulus $\tilde{K}_{eq}(\omega)$ from the Johnson-Champoux-Allard model [35, 36].

The interface and boundary conditions are listed from bottom to top: at $x_2 = 0$ lies the bottom boundary Γ_0 of the poroelastic domain, which is rigid or a Dirichlet-type boundary condition and thus,

$$\mathbf{u}^{(2)}(\Gamma_0) = 0; \quad \mathbf{u}^{f(p)}(\Gamma_2) \cdot \mathbf{n} - \mathbf{u}^{s(p)}(\Gamma_2) \cdot \mathbf{n} = 0.\tag{17}$$

Between the elastic and poroelastic domains, the interface is described as a total stress tensor of the poroelastic medium continuous at the interface Γ_1 with the stress tensor of the elastic solid and is expressed as $\boldsymbol{\sigma}^t = \hat{\boldsymbol{\sigma}}^s + (\phi\hat{\beta} - \tilde{\gamma})p\mathbf{I}$. The corresponding continuity equations are [37]

$$\boldsymbol{\sigma}^{(e)}(\Gamma_1) = \boldsymbol{\sigma}^{t(p)}(\Gamma_1); \quad \mathbf{u}^{(e)}(\Gamma_1) = \mathbf{u}^{s(p)}(\Gamma_1); \quad \mathbf{u}^{f(p)}(\Gamma_1) \cdot \mathbf{n} - \mathbf{u}^{s(p)}(\Gamma_1) \cdot \mathbf{n} = 0.\tag{18}$$

Finally, the elastic - fluid interface Γ_2 is accounted at $x_2 = h_1 + h_2 = H$, and the set of equation is

$$\sigma_{22}^{(1)} = -p^{(0+)}; \quad \sigma_{12}^{(1)} = 0; \quad u_2^{(1)} = u_2^{(0+)}\tag{19}$$

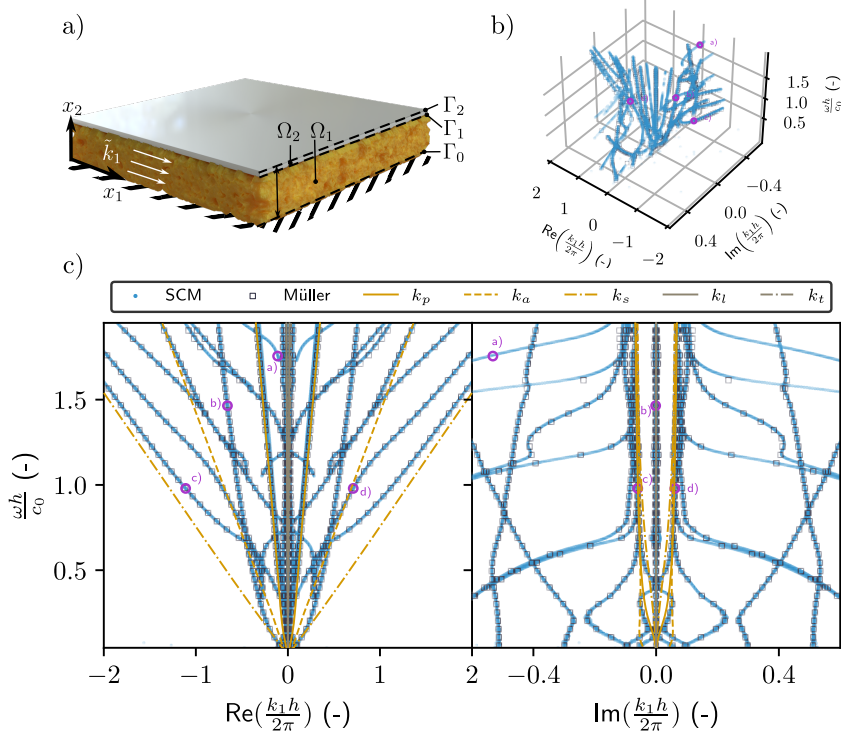


Figure 2: a) Diagram of the bilayer structure with its nomenclature and validated results with the SCM and Müller method comparison b) 3D view c) 2d plots with real and imaginary parts separated.

The whole system thus writes as

$$\begin{pmatrix} \boldsymbol{\Gamma}_0 & 0 & 0 \\ \boldsymbol{\alpha}_1 & 0 & 0 \\ \boldsymbol{\Gamma}_1^- & \boldsymbol{\Gamma}_1^+ & 0 \\ 0 & \boldsymbol{\alpha}_2 & 0 \\ 0 & \boldsymbol{\Gamma}_2^- & \boldsymbol{\Gamma}_2^+ \end{pmatrix} \begin{pmatrix} \mathbf{s}^{(p)} \\ \mathbf{s}^{(e)} \\ A_{0+} \end{pmatrix} = \mathbf{0}. \quad (20)$$

The details on the elements of each matrices $\boldsymbol{\Gamma}_i, i = 0, 1, 2$ and discretized motion equations $\boldsymbol{\alpha}_i, i = 0, 1$ is given in Appendix B.

4.2 Results

Once the numerical scheme is written and put in the form of Eq.12, we obtain a solution that is, at a given frequency, a set of eigenvalues γ and associated eigenvectors \mathbf{S} . Thus, we obtain \tilde{k}_1 by reverting the change of variable, which are complex values. Over a range of frequencies ω , the computation of the SCM for this bilayer structure yields its dispersion curve. Yet, part of the eigenvalues obtained from Eq. (13) need to be sorted out. Indeed, only wavenumbers corresponding to an outgoing fluid radiation with an exponentially decreasing amplitude fulfill the assumptions considered at the local interfaces. Thus, proper sorting of the wavenumber solution need to be considered [38] especially when a structure is fluid-loaded on both sides.

The results are presented in Fig.(2), as a complex 3D dispersion diagram. Real and Imaginary parts are depicted in Fig.(2c). The results of the SCM are plotted alongside results from the Müller method. Root-finding yields an analytical solution and using the SCM solution as the initial guesses for the method allows to get the full branches of the diagram, and allows to validate the present method. Overall, the results are comparable to Ref.[4] where the dispersion curves are studied at low frequencies, with wavenumbers close to 0. In the present study, the PEM is homogeneous and loaded with an aluminium plate; we observe a similar behavior which is due to the PEM nature. The various mode conversions and cutoffs frequencies originate from the viscothermal losses.

Branches with a very high slope and a low imaginary part are modes originating from waves propagating in the aluminium plate; these branches follow the same wavenumber as the one of its longitudinal k_l and transverse waves k_t . Considering the real part only, the various branches resemble lossy Lamb modes in their high-frequency behavior, when the thickness of the plate becomes larger than the wavelength [39], the slope of the branches grows proportionnaly to their main wave component whether the mode is mainly excited by the acoustic k_a , the compression k_p or the shear k_s wave of the poroelastic medium. Because of the rigid-backing at the bottom. The lowest order mode that would appear in a Lamb-like configuration is not excited here, . In another configuration shown in Appendix A, this mode can be seen in the dispersion diagram. However, with $\text{Re}(k_1) \rightarrow 0$, the structure exhibits

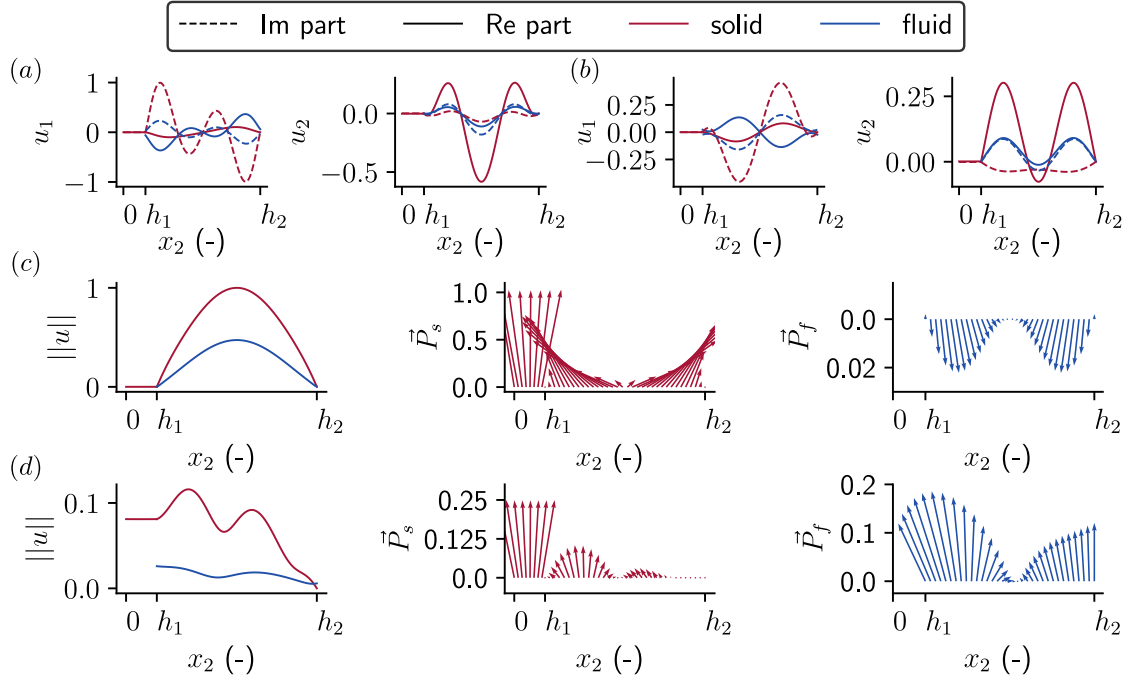


Figure 3: Fields solved from the SCM (a-b) displacements field of the solid and fluid phases of the structure with real (-) and imaginary (-) parts represented. (c-d) norm of the displacement vector of the fields and the Poynting vectors of the solid phases and fluid part.

a complex structure of branches

At each point of the dispersion curves solved using the method, there is an associated set of eigenvectors, representing the mode shapes of the solution for each physical field. Some of the mode shapes are represented in Fig.(3) and each subplot depicts the solution at its associated locii represented in magenta dots in Fig.(2c).

Focusing on Fig.(3a, 3b), the solid and fluid displacement fields are represented at two location on the dispersion diagram. The fluid phase displacement is computed from the pressure and solid displacement field using that $\mathbf{u}_f = \phi / (\tilde{\rho}_{22}\omega^2) \nabla p - \tilde{\rho}_{12}/\tilde{\rho}_{22} \mathbf{u}_s$.

Param.	Unit	Value
h_1	mm	52
ϕ	-	0.98
ρ_s	kg/m ³	6.5
σ	kPa.s/m ²	5.6
Λ	μm	214
Λ'	μm	214
α_∞	-	1
ν	-	0.24
N_s	kPa	11.96
η_s	Pa	72

Table 1: Parameters of the melamine foam

4.3 Repartitions of the solid and fluid energy contributions to the modal behaviour of the bilayer configuration

In this section, the dispersion diagram obtained from the SCM are investigated by using a method to calculate the Umov-Poynting vectors [40, 41] of elastic and poroelastic media, which represents the direction of the energy density in the structure. The tentative of a decoupled formulation to obtain the energy density of the waves propagating in the different phases of the PEM, elastic and fluid. The Umov-Poynting vector is written as

$$\mathbf{P} = -\frac{1}{2}\boldsymbol{\sigma}\mathbf{v}^*, \quad (21)$$

with $\boldsymbol{\sigma}$ the stress tensor and \mathbf{v}^* the particle velocity. These physical quantities are decoupled as for the total stress tensor, we can write $\boldsymbol{\sigma}_T = \boldsymbol{\sigma}_s + \boldsymbol{\sigma}_f$, which is decoupled in term of its solid and fluid phases contributions. In the same way, the total velocity can be written in the same way and two different expressions given in Appendix C allows to calculate \mathbf{P}_f the fluid phase Poynting vector and \mathbf{P}_s the solid phase Poynting vector.

Even though it would be interesting to further decouple the wave contributions

into compression and shear waves in the solid phase, as done in Ref.[42]. This is due to the presence of interfaces in the considered geometry, inducing mode conversions between the P and S waves.

The results are shown in Fig. (3c,3d) and show a normalized direction for each phase. For the point c), localized on the lowest-order propagating branch, in the quadrant of \tilde{k}_1 with $-\text{Re}, -\text{Im}$, the energy direction of the fluid and solid phase are opposite and have different dynamics in the case of the PEM layer. Even though there is no apparent modal contributions of the elastic plate in the dispersion diagram for the given frequency range, still an important amount of energy is localized therein.

5 Experimental confrontation

The results of the SCM are put to test by comparing them with experimental results. Retrieving dispersion relations of poroelastic panels can be quite tedious, and we set about to use the SLaTCoW method [43]. This method uses displacement fields scans along a line of length L . A 2D Laplace transform of these measurements is done. Then, assuming that plane waves are traveling in the sample with an expression $\zeta(x) = \sum_i \tilde{A}_s^i e^{i\tilde{k}_s^i x}; \forall x \in [0, L]$, an optimization on the amplitude A_s^i and complex wavenumbers \tilde{k}_s^i is performed using the Laplace transform of the experimental data.

The sample for this experiment is a bilayer structure of 45 by 85 cm, with an aluminium plate with $h_2 = 1$ mm stacked and glued on top of a yellow melamine foam with $h_1 = 52$ mm. The upper elastic coating is made of aluminium ($\rho = 2700$ kg/m³, $\lambda = 60.75$ GPa and $\mu = 26.03$ GPa) with thickness $h_2 = 1$ mm. The poroelastic materials is a melamine foam with parameters given in Tab. 1. The shear modulus includes a structural loss factor η_s with the form $\tilde{N}_s = N_s - i \cdot \eta_s$. The surrounding medium fluid is air ($c_0 = 343$ m/s, $\rho_f = 1.213$ kg/m³). The sample is rigidly-backed by a 3cm-thick aluminium plate, and positioned horizontally with the largest side on the floor.

The excitation of the sample is done via a shaker (Brüel and Kjaer type 4810) onto which is attached a metal plate glued to the edge of the poroelastic layer, used

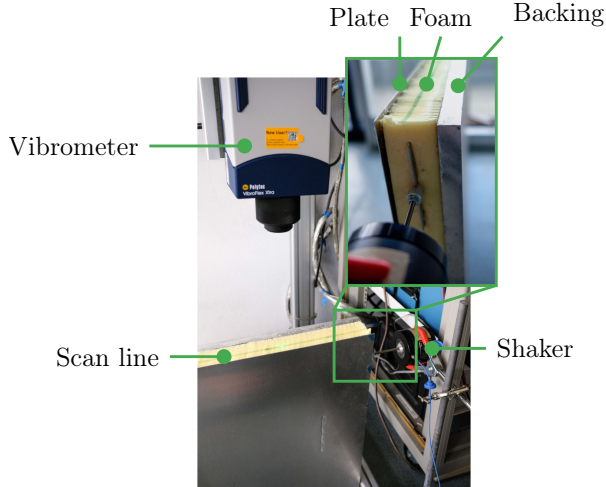


Figure 4: Experimental apparatus used for the measurement of the dispersion diagram of the bilayer structure. The normal displacement from the shaker excitation is measured across the thickness of the melamine foam using a laser vibrometer.

to make the line excitation in the sample. The excitation signal emitted is a swept-sine function with 400 points going from 500 Hz to 4 kHz. The upper limit of the frequency range corresponds to the first resonance frequency of the system formed by the metal rod attached to the shaker. These measurements are averaged 7400 times. The acquisition of the normal displacement of the sample is done using a laser Doppler vibrometer (Polytec VibroFlex Neo) on a line with length $L = 40$ cm, along the side of the thickness of the porous layer. The excitation signal and the measured field is interfaced through a computer via a Zürich Instruments acquisition card.

The results from the SLaTCoW method are shown in Fig. (5). Results are compared with SCM results. The configuration is the same as Fig. (2c) on a different frequency range, here from 1 to 3 kHz. Modes are sorted with a simple nearest neighbor algorithm, in order to follow each branch in the whole complex plane and are denoted with an index from 0 to 6 associated to the branch color which highlights its behavior in the complex plane.

Generally, we see that the solution extracted from the experimental data follows

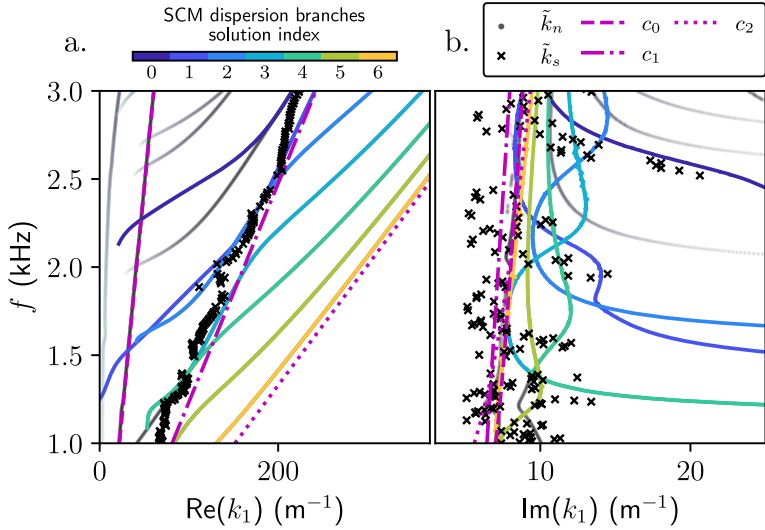


Figure 5: Experimental results with the a) real part and b) imaginary part of the wavenumber retrieved from the SLaTCoW method. The complex wavenumbers from the experiment are black crosses. The colored lines corresponds to modes from the SCM which are of interest, the remaining part of the solution are gray dots. The 3 Biot waves with velocities c_i , $i = 0 \dots 3$ are depicted in magenta.

some part of the branches that are close to the wavenumber corresponding to the solid compression wave in the PEM layer, especially with the real part, where there are jumps between various sections of the solution. The imaginary part of the measured data corresponds to the attenuation of the excitation signal inside of the structure. We generally retrieve the correct order of magnitude in this frequency range. However, the measured imaginary part

Part of several modes can be recovered with this technique. Only one solution is provided in the figure. The method was run to retrieve three modes in total in order to remove the remaining contributions that could be found in the normal displacement spectrum. The imaginary part of the recovered wavenumbers is an especially difficult task since almost a dozen modes theoretically exists in this frequency range and the large dissipations that occur in the system makes it intrinsically difficult to measure. Overlapping branches seen from the SCM solution in such a thin interval of the attenuation amount make it very difficult to measure precisely.

6 Conclusion

In the present work, we have developed a method to compute the dispersion diagrams of guided waves propagating in general multilayer structures, allowing for arbitrary arrangements of elastic, poroelastic and fluid layer. Outside fluid radiation is also taken into account. The SCM is used to discretize the motion equations describe the physical fields involved for each layer. Coupling interfaces and boundary conditions are also implemented. The solution allows to plot the full dispersion diagram in the considered structure, with complex wavenumbers. The physical fields of each layer are also retrieved in the form of eigenvectors, associated to the dispersion solution. Root-finding methods allow to validate SCM results. This allows for the analysis of dispersion properties in such structures, as well as other informations, such as the energy density direction in each phase of poroelastic layers using decoupled expression for Umov-Poynting vectors. An attempt to experimentally obtain similar results show that not all theoretical modes can be excited in experimental conditions. An extension of this method could be developed to model periodic systems by embedding inclusions (solid or resonant) in the layer and account the multiple scattering phenomena brought by periodic inclusions.

Appendices

A Case of the fluid-coupled poroelastic plate

In the following, a system similar to the one presented in the previous section is considered. Let a single layer of PEM surrounded by a fluid medium on each side. The system is thus symmetric and the guided waves propagation can be seen as leaky Lamb waves [44] that exist in elastic plates. See Fig.(6a) for a diagram.

With this configuration, the same method as described before to account for a fluid coupling at the interfaces Γ_0 and Γ_1 and discretize the poroelastic material governing equations. The latter will be given in greater details in this section. The fields acting on the domain Ω_1 are the ones from the (\mathbf{u}_s, p) formulation, the vector of

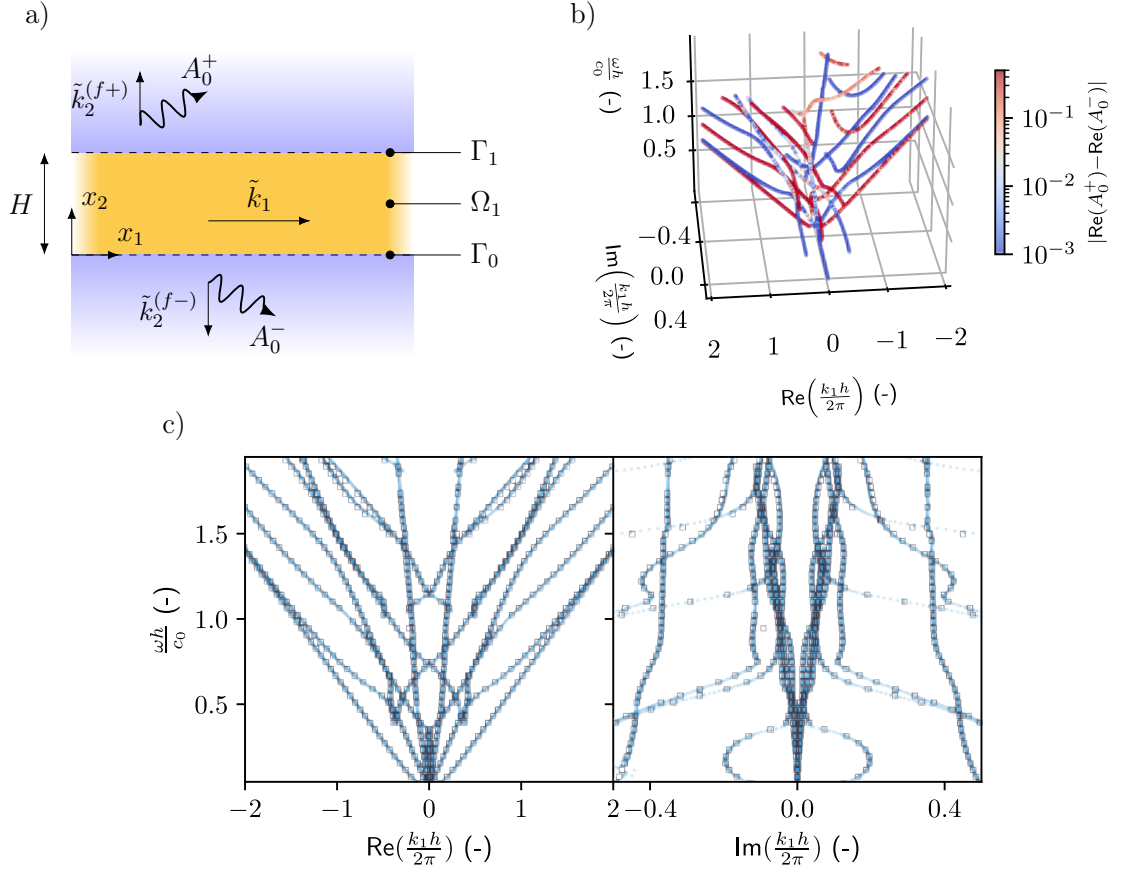


Figure 6: a) Diagram of the configuration with a fluid-coupled poroelastic layer (yellow rectangle) to infinite extent along x_1 with radiated amplitude at both edges. b) Dispersion diagram of the layer with a color-coding representing the symmetry and antisymmetry of the different presented branches. c) Comparison between the SCM simulations (blue dots) and analytical obtained with Müller method (black squares)

fields is thus $\mathbf{s}^{(p)} = (\mathbf{u}_{1,s}^p, \mathbf{u}_{2,s}^p, p^p)$. Using the analytical form of the motion equations given in Eq.(16), the discretization gives the matrix system,

$$\boldsymbol{\alpha}^{(p)} \mathbf{s}^{(p)} = \begin{pmatrix} (\omega^2 \tilde{\rho} - k_1^2 \hat{P}) \mathbf{T} + N_s \mathbf{T}_{22} & ik_1(\hat{P} - N_s) \mathbf{T}_2 & -ik_1 \tilde{\gamma} \mathbf{T} \\ ik_1(\hat{P} - N_s) \mathbf{T}_2 & \hat{P} \mathbf{T}_{22} + (\omega^2 \tilde{\rho} - k_1^2 N_s) \mathbf{T} & \tilde{\gamma} \mathbf{T}_2 \\ -ik_1 \tilde{\gamma} \mathbf{T} & -\tilde{\gamma} \mathbf{T}_2 & \left(\frac{\phi^2}{R} - \frac{\phi^2 k_1^2}{\tilde{\rho}_{22} \omega^2}\right) \mathbf{T} \end{pmatrix} \mathbf{u}^{(p)} = 0. \quad (22)$$

The various coefficients expressed above originates from the Biot theory and the (\mathbf{u}_s, p) formulation and are [34, 45],

$$\begin{aligned} \hat{P} &= \hat{A} + 2N_s, \quad \hat{A} = \tilde{A} - \frac{\tilde{Q}^2}{\tilde{R}}, \quad \tilde{\rho} = \rho_{11} - \frac{\tilde{\rho}_{12}^2}{\tilde{\rho}_{22}}, \\ \tilde{\gamma} &= \phi \left(\frac{\tilde{\rho}_{12}}{\tilde{\rho}_{22}} - \frac{\tilde{Q}}{\tilde{R}} \right), \quad \hat{\beta} = 1 + \frac{\tilde{\rho}_{12}}{\tilde{\rho}_{22}}; \end{aligned} \quad (23)$$

where N_s is the solid material shear modulus, ϕ the porosity. \hat{P}, \hat{Q} and \hat{R} are the so-called Biot coefficients and the effective densities are $\tilde{\rho}_{11}, \tilde{\rho}_{12}$ and $\tilde{\rho}_{22}$.

Next, the interfaces conditions are described. These interfaces are denoted as in Fig.(6a) with Γ_0 at $x_2 = 0$ and Γ_1 at $x_2 = H$, respectively the lower and upper interfaces. In both cases, the set of equations are those of a fluid-poroelastic interface given as [37]

$$\begin{aligned} (1 + \phi \hat{\beta}) u_2^{(1)} + \frac{\phi^2}{\tilde{\rho}_{22} \omega^2} \partial_2 p^{(1)} &= u_2^{(0\pm)}; \\ p^{(1)} &= p^{(0\pm)}; \quad \hat{\sigma}_{22}^s = (\phi \hat{\beta} - 1 - \tilde{\gamma}) p^{(0\pm)}; \quad \hat{\sigma}_{12}^s = 0. \end{aligned} \quad (24)$$

In discretized form, it yields the following matrix for the upper condition (with a radiated wave decreasing towards $x_2 \rightarrow +\infty$).

$$\underline{\underline{\Gamma}}_1 = \begin{pmatrix} \frac{\phi^2}{\tilde{\rho}_{22} \omega^2} T_2(H) & 0 & (1 + \phi \hat{\beta}) \underline{T}(H) & \frac{ik_2^{(f)}}{\rho_f \omega^2} \\ \underline{T}(H) & 0 & 0 & -1 \\ 0 & ik_1(\hat{P} - 2N_s) \underline{T}(H) & \hat{P} \underline{T}_2(H) & 1 + \tilde{\gamma} - \phi \hat{\beta} \\ 0 & N_s \underline{T}_2(H) & ik_1 N_s \underline{T}(H) & 0 \end{pmatrix}. \quad (25)$$

Taking a number of fields $P_1 = 3$ and a number of collocation points $M_1 = M$ for the layer makes the problem size $3M + 2$ (with 2 amplitudes terms for the radiated waves).

Those matrices are then arranged alike the system of Eq.(6) and the wavenumbers are solved as derived in the method. One ends up with the results in Fig.(6c). These results are from a configuration with a melamine foam (same as before) with $H = 0.1\text{m}$ coupled with air. The procedure is the same as in the previous results: the comparison between the SCM simulations and the Müller method shows matching results for all of the branches over the frequency range.

An additionnal analysis can be done here, because of the symmetry of the geometry: the modes of the system can be segregated into symmetric and antisymmetric modes as is done to study classical Lamb waves in plates. However, this decoupling is done usually done analytically. In the present work, we represent the difference in radiated wave amplitudes at each side at the plate, as $|\text{Re}(A_0^+) - \text{Re}(A_0^-)|$. These results are shown in Fig. (6b) Symmetric modes would see this value go towards 0 and are represented in blue whereas antisymmetric modes would have an noticeable difference for both wave amplitudes (red branches). Considering only the real plane, these results are analogous to what is found for Lamb modes [39]. Nevertheless, no modes exists solely in the real plane in this configuration: from the viscothermal dissipations in the PEM, there always exists a contributing imaginary part in the wavenumber solution. All branches in the imaginary quadrant of the solution are contributed from the PEM layer and not from the fluid-coupling. Small radiations are occuring at the interface, but the effect is not as strong as if it was a heavy fluid, saturating the surrounding medium and the pores of the layer.

B Expressions for different types of layers

B.1 Discretized governing equations

- Equivalent fluid $\left(\underline{\underline{D}}_{22,f} + \tilde{k}_{eq}^2 \underline{\underline{I}}_f\right) \underline{p} = 0$

- Poroelastic layer

$$\begin{pmatrix} (\omega^2 \tilde{\rho} - k_1^2 \hat{P}) \underline{\underline{I}} + N_s \underline{\underline{D}}_{22} & ik_1(\hat{P} - N_s) \underline{\underline{D}}_2 & -ik_1 \tilde{\gamma} \underline{\underline{I}} \\ ik_1(\hat{P} - N_s) \underline{\underline{D}}_2 & \hat{P} \underline{\underline{D}}_{22} + (\omega^2 \tilde{\rho} - k_1^2 N_s) \underline{\underline{I}} & \tilde{\gamma} \underline{\underline{D}}_2 \\ -ik_1 \tilde{\gamma} \underline{\underline{I}} & -\tilde{\gamma} \underline{\underline{D}}_2 & \left(\frac{\phi^2}{R} - \frac{\phi^2 k_1^2}{\tilde{\rho}_{22} \omega^2} \right) \underline{\underline{I}} \end{pmatrix} \begin{pmatrix} \underline{u}_{1,p} \\ \underline{u}_{2,p} \\ p_p \end{pmatrix} = \underline{0}, \quad (26)$$

- Elastic layer

$$\left[\rho^{(e)} \omega^2 \underline{\underline{I}} + \begin{pmatrix} -k_1^2(\lambda + 2\mu) \underline{\underline{I}} + \mu \underline{\underline{D}}_{22} & ik_1(\lambda + \mu) \underline{\underline{D}}_2 \\ ik_1(\lambda + \mu) \underline{\underline{D}}_2 & (\lambda + 2\mu) \underline{\underline{D}}_{22} - k_1^2 \mu \underline{\underline{I}} \end{pmatrix} \right] \begin{pmatrix} \underline{u}_{1,e} \\ \underline{u}_{2,e} \end{pmatrix} = 0. \quad (27)$$

B.2 Boundary and coupling conditions

Interface conditions at Γ_1 between elastic $\Omega^{(1)}$ and PEM $\Omega^{(2)}$. In the interface, only one row of the matrices are taken, which index corresponds to their position (first row of the matrix if the coupled layer is at the bottom, or last row if the layer is above),

- Elastic-fluid coupling: $\underline{\underline{\Gamma}}_{e-f} \underline{s}_{e-f} = 0$, with $\underline{s}_{e-f} = (\underline{u}_{1,e} \ \underline{u}_{2,e} \ \underline{p}_f)^T$ and,

$$\underline{\underline{\Gamma}}_{e,f} = \begin{pmatrix} \underline{\underline{D}}_{2,e} & ik_1 \underline{I}_e & 0 \\ ik_1 \lambda \underline{I}_e & (\lambda + 2\mu) \underline{\underline{D}}_{2,e} & \underline{I}_f \\ \underline{0} & \underline{I}_e & -ik_{2,f}/(\rho_f \omega^2) \underline{I}_f \end{pmatrix}. \quad (28)$$

- Poroelastic-elastic coupling : $\underline{\underline{\Gamma}}_e^- \underline{s}_e + \underline{\underline{\Gamma}}_p^+ \underline{s}_p = \underline{\underline{\Gamma}}_{p-e} \begin{pmatrix} \underline{u}_{1,e} & \underline{u}_{2,e} & \underline{p}_p & \underline{u}_{1,p} & \underline{u}_{2,p} \end{pmatrix}^T = 0$

$$\underline{\underline{\Gamma}}_{p,e} = \begin{pmatrix} \mu \underline{\underline{D}}_{2,e} & ik_1 \mu \underline{I}_e & -N_s \underline{\underline{D}}_{2,p} & -ik_1 N_s \underline{I}_p & \underline{0} \\ ik_1 \lambda \underline{I}_s & (\lambda + 2\mu) \underline{\underline{D}}_{2,e} & -ik_1 (\hat{P} - 2N_s) \underline{I}_p & -\hat{P} \underline{\underline{D}}_{2,p} & \phi \left(1 + \frac{\tilde{Q}}{R} \right) \underline{I}_p \\ -\underline{I}_e & \underline{0} & \underline{0} & \underline{I}_p & \underline{0} \\ \underline{0} & -\underline{I}_e & \underline{0} & \underline{0} & \underline{I}_p \\ \underline{0} & \underline{0} & \frac{\phi}{\tilde{\rho}_{22} \omega^2} \underline{\underline{D}}_{2,p} & -\hat{\beta} \underline{I}_p & \underline{0} \end{pmatrix} \quad (29)$$

- Fluid-poroelastic coupling

$$\underline{\underline{\Gamma}}_{p,f} = \begin{pmatrix} -\frac{ik_2^{(f)}}{\rho_f \omega^2} & \frac{\phi^2}{\tilde{\rho}_{22}\omega^2} \underline{D}_{2,p} & \underline{0} & (1 + \phi\hat{\beta}) \underline{I}_p \\ -1 & \underline{I} & \underline{0} & \underline{0} \\ 1 + \tilde{\gamma} - \phi\hat{\beta} & \underline{0} & ik_1(\hat{P} - 2N_s) \underline{I}_p & \hat{P} \underline{D}_{2,p} \\ 0 & \underline{0} & N_s \underline{D}_{2,p} & ik_1 N_s \underline{I}_p \end{pmatrix} \quad (30)$$

- Rigid poroelastic boundary

$$\underline{\underline{\Gamma}}_{p,r} \underline{s}_p = \begin{pmatrix} \underline{0} & \underline{I}_p & \underline{0} \\ \underline{0} & \underline{0} & \underline{I}_p \\ \frac{\phi}{\tilde{\rho}_{22}\omega^2} \underline{D}_{2,p} & \underline{0} & -\hat{\beta} \underline{I}_p \end{pmatrix} \begin{pmatrix} \underline{p}_p \\ \underline{u}_{1,p} \\ \underline{u}_{2,p} \end{pmatrix} = \underline{0} \quad (31)$$

C Decoupling of Umov-Poynting vectors: separation fluid and solid phases

Using the mode shapes solved from the SCM, we obtained the fields representing the propagation of the waves in each layer of material. These fields allow us to compute a number of physical quantities, among which the Umov-Poynting vector defined as $\mathbf{P} = -\frac{1}{2}\boldsymbol{\sigma}\mathbf{v}^*$ with $\boldsymbol{\sigma}$ the stress tensor of the poroelastic medium and \mathbf{v} the velocity vector. As the separations,

$$\boldsymbol{\sigma}_T = \boldsymbol{\sigma}_s + \boldsymbol{\sigma}_f, \quad \mathbf{v}_T = \mathbf{v}_s + \mathbf{v}_f \quad (32)$$

are done, we end up with separated \mathbf{P}_s and \mathbf{P}_f . Since these quantities are decoupled, the cross product vanishes.

In the poroelastic layers, we separate the previous expression in the contributions for the solid phase of the Umov-Poynting vectors

$$\mathbf{P}_s = -\frac{1}{2}\boldsymbol{\sigma}_s \mathbf{v}_s^*, \quad (33)$$

with the stress tensor from the solid phase [34].

$$\boldsymbol{\sigma}_s = \underbrace{\hat{A} \nabla \cdot \mathbf{u}_s \mathbf{I} + 2\tilde{N}_s \boldsymbol{\epsilon}_s}_{\hat{\boldsymbol{\sigma}}_s} - \phi \frac{\tilde{Q}}{\tilde{R}} p \mathbf{I}. \quad (34)$$

In this equation, $\hat{\boldsymbol{\sigma}}_s$ represents the *in-vacuo* solid stress tensor with the term in p coupling the solid displacement with the pressure field .

$$\boldsymbol{P}_f = -\frac{1}{2} \boldsymbol{\sigma}_f \boldsymbol{v}_f^* \quad (35)$$

The fluid velocity \boldsymbol{v}_f is derived from the fluid displacement field,

$$\boldsymbol{u}_f = \frac{\phi}{\tilde{\rho}_{22}\omega^2} \boldsymbol{\nabla} p - \frac{\tilde{\rho}_{12}}{\tilde{\rho}_{22}} \boldsymbol{u}_s. \quad (36)$$

References

- [1] T. Weisser et al. "Acoustic Behavior of a Rigidly Backed Poroelastic Layer with Periodic Resonant Inclusions by a Multiple Scattering Approach". *J. Acoust. Soc. Am.* 139.2 (2016), pp. 617–629.
- [2] L. Boeckx et al. "Investigation of the Phase Velocities of Guided Acoustic Waves in Soft Porous Layers". *J. Acoust. Soc. Am.* 117.2 (2005), pp. 545–554.
- [3] G. Belloncle et al. "Normal Modes of a Poroelectric Plate and Their Relation to the Reflection and Transmission Coefficients". *Ultrasonics* 41.3 (2003), pp. 207–216.
- [4] D. Gusakov and A. Vatul'yan. "Dispersion Properties of Inhomogeneous Poroelastic Layer". *Z Angew Math Mech* 98.4 (2018), pp. 532–541.
- [5] D. E. Muller. "A Method for Solving Algebraic Equations Using an Automatic Computer". *Mathematical Tables and Other Aids to Computation* 10.56 (1956), p. 208.
- [6] P. Kowalczyk and W. Marynowski. "Efficient Complex Root Tracing Algorithm for Propagation and Radiation Problems". *IEEE Trans. Antennas Propagat.* 65.5 (2017), pp. 2540–2546.
- [7] L. Wan. *A New Method to Find Full Complex Roots of a Complex Dispersion Equation for Light Propagation*. Comment: 9pages,5figures. 2011. url: <http://arxiv.org/abs/1109.0879> (visited on 11/23/2023). preprint.
- [8] J. R. Pinkert. "An Exact Method for Finding the Roots of a Complex Polynomial". *ACM Trans. Math. Softw.* 2.4 (1976), pp. 351–363.
- [9] B. Yang, D. Gottlieb, and J. Hesthaven. "Spectral Simulations of Electromagnetic Wave Scattering". *Journal of Computational Physics* 134.2 (1997), pp. 216–230.
- [10] V. Pagneux and A. Maurel. "Determination of Lamb Mode Eigenvalues". *J. Acoust. Soc. Am.* 110.3 (2001), pp. 1307–1314.
- [11] A. T. I. Adamou and R. V. Craster. "Spectral Methods for Modelling Guided Waves in Elastic Media". *J. Acoust. Soc. Am.* 116.3 (2004), pp. 1524–1535.
- [12] F. Karpfinger, B. Gurevich, and A. Bakulin. "Modeling of Wave Dispersion along Cylindrical Structures Using the Spectral Method". *J. Acoust. Soc. Am.* 124.2 (2008), pp. 859–865.
- [13] F. H. Quintanilla, M. J. S. Lowe, and R. V. Craster. "Modeling Guided Elastic Waves in Generally Anisotropic Media Using a Spectral Collocation Method". *J. Acoust. Soc. Am.* 137.3 (2015), pp. 1180–1194.
- [14] M. Gallezot, F. Treyssède, and L. Laguerre. "Contribution of Leaky Modes in the Modal Analysis of Unbounded Problems with Perfectly Matched Layers". *The Journal of the Acoustical Society of America* 141.1 (2017), EL16–EL21.
- [15] E. Georgiades, M. J. S. Lowe, and R. V. Craster. "Leaky Wave Characterisation Using Spectral Methods". *J. Acoust. Soc. Am.* 152.3 (2022), pp. 1487–1497.
- [16] D. A. Kiefer et al. "Calculating the Full Leaky Lamb Wave Spectrum with Exact Fluid Interaction". *J. Acoust. Soc. Am.* 145.6 (2019), pp. 3341–3350.
- [17] I. Bartoli et al. "Modeling Wave Propagation in Damped Waveguides of Arbitrary Cross-Section". *Journal of Sound and Vibration* 295.3-5 (2006), pp. 685–707.
- [18] A. Marzani et al. "A Semi-Analytical Finite Element Formulation for Modeling Stress Wave Propagation in Axisymmetric Damped Waveguides". *Journal of Sound and Vibration* 318.3 (2008), pp. 488–505.
- [19] F. Treyssède et al. "Finite Element Computation of Trapped and Leaky Elastic Waves in Open Stratified Waveguides". *Wave Motion* 51.7 (2014), pp. 1093–1107.
- [20] M. Lowe. "Matrix Techniques for Modeling Ultrasonic Waves in Multilayered Media". *IEEE Trans. Ultrason., Ferroelect., Freq. Contr.* 42.4 (1995), pp. 525–542.
- [21] N. A. Haskell. "The Dispersion of Surface Waves on Multilayered Media^a". *Bulletin of the Seismological Society of America* 43.1 (1953), pp. 17–34.
- [22] G. Song, Z. Mo, and J. S. Bolton. "A General and Stable Approach to Modeling and Coupling Multilayered Acoustical Systems with Various Types of Layers". *J. Sound Vib.* (2023), p. 117898.
- [23] M. Huang, F. Cegla, and B. Lan. "Stiffness Matrix Method for Modelling Wave Propagation in Arbitrary Multilayers". *International Journal of Engineering Science* 190 (2023), p. 103888.
- [24] C. Canuto, ed. *Spectral Methods: Fundamentals in Single Domains ; with 19 Tables*. Scientific Computation. Berlin Heidelberg New York: Springer, 2006. 563 pp.
- [25] L. N. Trefethen. *Spectral Methods in MATLAB*. Society for Industrial and Applied Mathematics, 2000.
- [26] W. S. Don and A. Solomonoff. "Accuracy and Speed in Computing the Chebyshev Collocation Derivative". *SIAM J. Sci. Comput.* 16.6 (1995), pp. 1253–1268.
- [27] J. A. Weideman and S. C. Reddy. "A MATLAB Differentiation Matrix Suite". *ACM Trans. Math. Softw.* 26.4 (2000), pp. 465–519.
- [28] R. Baltensperger and M. R. Trummer. "Spectral Differencing with a Twist". *SIAM J. Sci. Comput.* 24.5 (2003), pp. 1465–1487.
- [29] T. Betcke et al. "NLEVP: A Collection of Nonlinear Eigenvalue Problems". *ACM Trans. Math. Softw.* 39.2 (2013), pp. 1–28.
- [30] A. Hood. "Localizing the Eigenvalues of Matrix-Valued Functions: Analysis and Applications" (2017).
- [31] J. D. Achenbach, H. A. Lauwerier, and W. T. Koiter. *Wave Propagation in Elastic Solids: North-Holland Series in Applied Mathematics and Mechanics*. Amsterdam: Elsevier Science, 2014.
- [32] M. A. Biot. "Theory of Propagation of Elastic Waves in a Fluid-Saturated Porous Solid. I. Low-Frequency Range". *J. Acoust. Soc. Am.* 28.2 (1956), pp. 168–178.

- [33] M. A. Biot. "Theory of Propagation of Elastic Waves in a Fluid-Saturated Porous Solid. II. Higher Frequency Range". *J. Acoust. Soc. Am.* 28.2 (1956), pp. 179–191.
- [34] N. Atalla, R. Panneton, and P. Debergue. "A Mixed Displacement-Pressure Formulation for Poroelastic Materials". *J. Acoust. Soc. Am.* 104.3 (1998), pp. 1444–1452.
- [35] D. L. Johnson, J. Koplik, and R. Dashen. "Theory of Dynamic Permeability and Tortuosity in Fluid-Saturated Porous Media". *J. Fluid Mech.* 176 (-1987), p. 379.
- [36] Y. Champoux and J.-F. Allard. "Dynamic Tortuosity and Bulk Modulus in Air-saturated Porous Media". *J. Appl. Phys.* 70.4 (1991), pp. 1975–1979.
- [37] P. Debergue, R. Panneton, and N. Atalla. "Boundary Conditions for the Weak Formulation of the Mixed (u,p) Poroelasticity Problem". *J. Acoust. Soc. Am.* 106.5 (1999), pp. 2383–2390.
- [38] D. A. Kiefer. "Elastodynamic Quasi-Guided Waves for Transit-Time Ultrasonic Flow Metering". FAU University Press, 2022, 15697 KB, xiv, 213 Seiten pages.
- [39] D. Royer and T. Valier-Brasier. *Ondes élastiques dans les solides*. Collection Ondes. London: ISTE éditions, 2021.
- [40] J. M. Carcione. "Wave Propagation in Anisotropic, Saturated Porous Media: Plane-wave Theory and Numerical Simulation". *J. Acoust. Soc. Am.* 99.5 (1996), pp. 2655–2666.
- [41] J. M. Carcione. *Wave Fields in Real Media - Wave Propagation in Anisotropic, Anelastic, Porous and Electromagnetic Media*. Vol. 38. Handbook of Geophysical Exploration: Seismic Exploration. Elsevier, 2007.
- [42] W. Wang et al. "Up/down and P/S Decompositions of Elastic Wavefields Using Complex Seismic Traces with Applications to Calculating Poynting Vectors and Angle-Domain Common-Image Gatherers from Reverse Time Migrations". *GEOPHYSICS* 81.4 (2016), S181–S194.
- [43] A. Geslain et al. "Spatial Laplace Transform for Complex Wavenumber Recovery and Its Application to the Analysis of Attenuation in Acoustic Systems". *J. Appl. Phys.* 120.13 (2016), p. 135107.
- [44] T. Plona, W. Mayer, and M. Behravesh. "Rayleigh and Lamb Waves at Liquid-Solid Boundaries". *Ultrasoundics* 13.4 (1975), pp. 171–175.
- [45] J.-F. Allard and N. Atalla. *Propagation of Sound in Porous Media: Modelling Sound Absorbing Materials*. 2nd ed. Hoboken, N.J: Wiley, 2009. 358 pp.